

Reconstructing Heterogeneous Biomolecules via Hierarchical Gaussian Mixtures and Part Discovery

Shayan Shekarforoush^{1, 2}
shayan@cs.toronto.edu

David B. Lindell^{1, 2}
lindell@cs.toronto.edu

Marcus A. Brubaker^{1, 2, 3}
mab@eecs.yorku.ca

David J. Fleet^{1, 2}
fleet@cs.toronto.edu

¹University of Toronto ²Vector Institute ³York University

Abstract

Cryo-EM is a transformational paradigm in molecular biology where computational methods are used to infer 3D molecular structure at atomic resolution from extremely noisy 2D electron microscope images. At the forefront of research is how to model the structure when the imaged particles exhibit non-rigid conformational flexibility and compositional variation where parts are sometimes missing. We introduce a novel 3D reconstruction framework with a hierarchical Gaussian mixture model, inspired in part by Gaussian Splatting for 4D scene reconstruction. In particular, the structure of the model is grounded in an initial process that infers a part-based segmentation of the particle, providing essential inductive bias in order to handle both conformational and compositional variability. The framework, called CryoSPIRE, is shown to reveal biologically meaningful structures on complex experimental datasets, and establishes a new state-of-the-art on CryoBench, a benchmark for cryo-EM heterogeneity methods. [Project Webpage](#).

1 Introduction

Single-particle cryo-electron microscopy (cryo-EM) is a computationally driven experimental paradigm that is transforming molecular biology by enabling 3D structure determination of biomolecules, such as proteins and viruses, at near-atomic resolutions [3, 18, 38]. The core computational task is estimating a 3D structure from 2D images with unknown orientation and position, under extremely low signal-to-noise conditions. Essential to their biological function, biomolecules exhibit varying degrees of *conformational flexibility*, where structures deform non-rigidly, and *compositional variation*, where parts of a structure may be present in some images and absent in others (see Fig. 1). Accordingly, a major challenge in cryo-EM is the estimation of 3D structures from such heterogeneous data and, to that end, how to infer meaningful representations of structures such as parts that capture their heterogeneity. The crux of this challenge is how to effectively represent and regularize this variability without overfitting to the noise in cryo-EM images. Existing methods, while encouraging, are generally limited in either expressiveness, interpretability, or efficiency.

Here, we propose CryoSPIRE, a new method for heterogeneous reconstruction. We leverage a part-based Gaussian mixture model (GMM) of 3D density that enables CryoSPIRE to represent both conformational and compositional heterogeneity, unlike some existing deformation-based methods [13, 33]. Further, it provides a naturally interpretable and physically plausible, part-based structure in contrast to existing latent variable methods based on linear density subspaces [10, 32] or neural field models [19, 20, 47]. A key challenge with part-based GMMs concerns initialization and the discovery of parts. We propose a novel method for part discovery which estimates a coarse-grained GMM with per-Gaussian learnable features (c.f., [2]) and an MLP which defines Gaussian locations and amplitudes. We show that these learned features naturally encode characteristics of structural

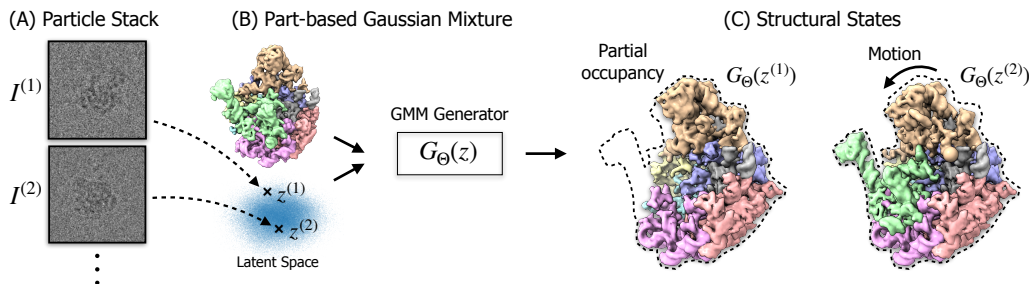


Figure 1: (A) Based on a stack of noisy particle images, (B) CryoSPIRE learns a part-based Gaussian mixture, with parameters Θ , and a latent space representing structural heterogeneity. Given a latent code z , a generator produces a 3D density map. (C) The model supports compositional variability (e.g., $G_{\Theta}(z^{(1)})$ with a missing part), and conformational flexibility (e.g., $G_{\Theta}(z^{(2)})$ with part deformation).

heterogeneity, which we leverage to infer a part-based segmentation of the structure. Inspired in part by Scaffold-GS [21], we define CryoSPIRE (Scaffold Part-Aware Mixture of Gaussians), a hierarchical model which estimates a Gaussian mixture wherein the composition of components and their deformation are defined in terms of a set of anchors, corresponding to parts. The resulting model naturally allows for the arbitrary combination of parts which can both rigidly move and locally deform as a function of an input heterogeneity latent code (see Fig. 1).

To our knowledge, this is first GMM-based model to be successfully benchmarked on CryoBench [15], a standardized benchmark for cryo-EM heterogeneity with ground-truth labels. In particular, CryoSPIRE outperforms widely used and state-of-the-art methods [10, 19, 32, 33, 47], sometimes by a wide margin. Through ablations, we also validate key design choices, demonstrating the benefits of Gaussian features over positional encoding as in DynaMight [40], and highlighting the benefits of hierarchical motion modeling. Finally, on real experimental cryo-EM data, CryoSPIRE automatically discovers representations of 3D density maps that correspond to biologically meaningful parts.

To summarize our contributions: we propose a new method enabling part-discovery on 3D biomolecular structures based on a coarse-grained GMM. This part-based structure is used to initialize a novel, hierarchical GMM-based model for heterogeneous reconstruction with compositional and conformational variability. The resulting framework, CryoSPIRE, establishes a new state-of-the-art on quantitative benchmarks and qualitative experimental datasets.

2 Background and Related Work

Latent Variable Models. Heterogeneous cryo-EM reconstruction methods typically introduce latent variables to represent structural variability of the 3D density map. 3DVA [32] and RECOVER [10] learn a linear subspace to represent variation in 3D density maps, with clever numerical and regularization techniques to optimize high-dimensional basis maps at high spatial resolutions. Such methods are often notoriously memory intensive and have limited expressiveness due to the linear subspace. Much current work has shifted to nonlinear latent models and deep learning [14, 19, 47], with Cryo-DRGN [47] and DRGN-AI [19] using auto-encoders to obtain latent codes and conditional coordinate networks [24] to generate density maps. Such latent-variable models are hard to interpret, however, as conformational and compositional heterogeneity are not decoupled, and they provide no explicit model of motion between conformational states. By contrast, the latents in 3DFlex [33] encode flow fields that model the conformational deformation of a canonical structure. While resolving detailed motion and improving the quality of density maps, 3DFlex cannot handle compositional heterogeneity, and it is highly sensitive to regularization, often requiring substantial trial and error.

GMM-Based Methods. Gaussian mixtures have been used to model 3D density [4, 5, 6, 40]; they provide a sparse, compact representation in which conformation and compositional variability are modeled in terms of positions and amplitudes of Gaussian components. With Gaussian components viewed as atomic primitives, such models also facilitate physics-based priors [6, 40] and subsequent molecular model fitting. Nevertheless, existing GMM-based methods fall short in various ways. E2GMM [4] and related methods [5, 6] generate GMM parameters with a single network, which scales poorly to large numbers of Gaussians. Further, their multi-scale smoothness priors [6] are based on an arbitrary hierarchy which fails to capture part-based structures, thus resorting to manual part masks to resolve and estimate local motions. DynaMight [40] is similar to CryoSPIRE in defining

an explicit motion model, but it is unable to handle compositional variations, and, as we show, its positional encodings are inferior to our learnable features.

Gaussian Splatting. Beyond cryo-EM, the effectiveness of GMMs has been demonstrated in 3D Gaussian Splatting [16, 48], a technique which provides a fast approximation to the volume rendering integral [8, 23], enabling efficient high-fidelity reconstruction of 3D scenes from multi-view images [11, 17, 22, 44, 45, 46]. 3D Gaussian Splatting represents scene appearance and structure using thousands to millions of Gaussian components, each associated with parameters that control opacity and view-dependent color. CryoSPIRE is in part inspired by Gaussian Splatting [2, 21], but tailored to cryo-EM, with a different image formation model, images with signal-to-noise ratios less than 5%, and a novel method for part discovery.

GMM Image Formation. Following [4, 5, 6, 40], we parameterize the terms of a Gaussian mixture with center $\mathbf{c} \in \mathbb{R}^3$, isotropic scale $s \in \mathbb{R}$, and an amplitude $m \in \mathbb{R}$:

$$f(\mathbf{p}) = \sum_i m_i \exp\left(-\frac{\|\mathbf{p} - \mathbf{c}_i\|_2^2}{2s_i^2}\right), \quad (1)$$

for location $\mathbf{p} \in \mathbb{R}^3$. We transform the GMM into the observation space for the n -th particle image, with a rotation $\mathbf{R}^{(n)} \in SO(3)$ and translation $\mathbf{t}^{(n)} \in \mathbb{R}^3$, followed by an integral projection along the z -axis of the microscope, to obtain a noise-free 2D image, $\tilde{I}(\tilde{\mathbf{p}})$, [4]:

$$\tilde{I}^{(n)}(\tilde{\mathbf{p}}) = \sum_i \sqrt{2\pi}s_i m_i \exp\left(-\frac{\|\tilde{\mathbf{p}} - [\mathbf{R}^{(n)} \mathbf{c}_i + \mathbf{t}^{(n)}]_{xy}\|_2^2}{2s_i^2}\right), \quad (2)$$

where $\tilde{\mathbf{p}} \in \mathbb{R}^2$ and $[\cdot]_{xy}$ is an operator to discard z coordinate of the input position. Cryo-EM images are then convolved with microscope point spread function and corrupted by additive mean-zero Gaussian noise, $\hat{I}^{(n)} = g^{(n)} \star \tilde{I}^{(n)} + \epsilon^{(n)}$. Like other cryo-EM models, the parameters are typically optimized by minimizing a squared L2 reconstruction loss between model predictions and observed images. See the supplement for more details on image formation and the image likelihood.

3 CryoSPIRE

Heterogeneous cryo-EM involves non-rigid 3D reconstruction from noisy 2D images. For such an inverse problem, regularization and inductive bias are key. Local smoothness is a natural choice for regularization, however, smoothness alone is not sufficient as nearby regions can deform in somewhat independent ways [33]. Further, the presence or absence of biomolecule parts is not dictated by spatial proximity alone. Macromolecular complexes, like many objects, naturally possess a part-based structure that connects to their compositional and conformational variations. But a coherent 3D part-decomposition is unavailable *a priori*, and estimating parts from noisy 2D observations is inherently challenging. As a consequence, prior work resort to manually designed masks or meshes [25, 33].

Here, we propose a novel two-stage GMM-based framework. Given particle images with corresponding poses $\{(I^{(n)}, \mathbf{R}^{(n)}, \mathbf{t}^{(n)})\}_{n=1}^N$, and a crude initial 3D structure, we first optimize a coarse-grained GMM in which each Gaussian component is augmented with a learnable feature vector (c.f., [2]). We observe that the learned features encode meaningful information about structural regularities. In particular, Gaussian components that coherently deform or consistently appear or disappear receive similar features, facilitating the inference of a part-based segmentation of the particle. Second, based on the identified parts and inspired by Scaffold-GS [21], we define a part-aware Gaussian mixture model in terms of a set of anchors, one per part, each with a corresponding set of Gaussians. Optimizing this representation recovers a high-resolution representation of 3D density maps with compositional and conformational variability. In what follows, we describe the part-based hierarchical model, (Fig. 2B–D), followed by the part discovery method and initialization scheme (Fig. 2A).

3.1 Part-Aware Gaussian Mixture

Our hierarchical model is conditioned on a latent coordinate $\mathbf{z} \in \mathcal{Z} \subset \mathbb{R}^D$ for each image, which specifies the state of the macromolecule. The density model itself comprises a set of anchors, each associated with a meaningful part of the macromolecule (Fig. 2B). We parameterize the anchors as, $\mathcal{A} = \{(\bar{\mathbf{c}}_a, \bar{\mathbf{f}}_a)\}_{a=1}^A$, where $\bar{\mathbf{c}}_a \in \mathbb{R}^3$ specifies the anchor center location in a canonical frame, and $\bar{\mathbf{f}}_a \in \mathcal{F} \subset \mathbb{R}^E$ is an associated feature vector that encodes heterogeneity information of its corresponding part. The GMM has G Gaussian components associated with anchors (Fig. 2B, left),

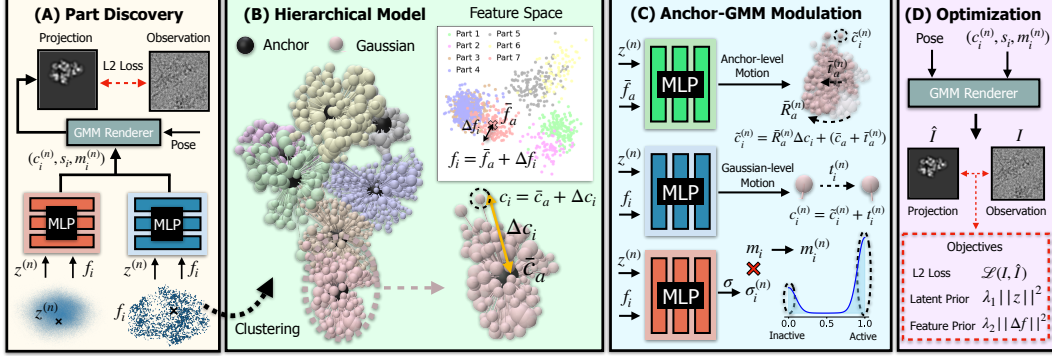


Figure 2: Overview of CryoSPIRE. **(A)** To infer parts, we optimize a coarse GMM with neural networks that generate Gaussian amplitudes and centers, conditioned on image latent codes and Gaussian features. **(B)** Clustering on learned Gaussian features provides meaningful parts. The CryoSPIRE model comprises one anchor and a set of Gaussians per part. **(C)** MLPs generate the rigid-body motion of each anchor (top), per-Gaussian displacements relative to the anchor frames (middle), and per-Gaussian activations in $(0,1)$ to represent occupancy (bottom). **(D)** A reconstruction loss compares observed images to 2D projection of the corresponding 3D GMM. Priors encourage bounded latent code and small feature offsets.

denoted by $\mathcal{G} = \{(\mathbf{f}_i, \mathbf{c}_i, s_i, m_i, a_i)\}_{i=1}^G$ where $\mathbf{f}_i \in \mathfrak{F}$ and $a_i \in \{1, \dots, A\}$ specifies the anchor associated with the Gaussian that is set by the part discovery method below. We parameterize the position and feature embedding of the i -th Gaussian relative to its associated anchor a_i as

$$\mathbf{c}_i = \bar{\mathbf{c}}_{a_i} + \Delta \mathbf{c}_i, \quad \mathbf{f}_i = \bar{\mathbf{f}}_{a_i} + \Delta \mathbf{f}_i, \quad (3)$$

where $\Delta \mathbf{c}_i \in \mathbb{R}^3$ and $\Delta \mathbf{f}_i \in \mathbb{R}^E$ are learnable offsets. We initially set $\Delta \mathbf{f}_i = \mathbf{0}$ so all Gaussians are initialized with the features of their corresponding anchors.

To enable conformational variability, we parameterize deformations at two levels. First, the large-scale motion of each anchor frame is parameterized as a rigid body transformation (Fig. 2C, top). Given the latent code for n -th particle image, $\mathbf{z}^{(n)} \in \mathfrak{Z}$, and the anchor feature vector $\bar{\mathbf{f}}_{a_i}$, we compute the rotated and translated center of the i -th Gaussian, $\tilde{\mathbf{c}}_i^{(n)}$, as

$$\tilde{\mathbf{c}}_i^{(n)} = \bar{\mathbf{R}}_{a_i}^{(n)} \Delta \mathbf{c}_i + (\bar{\mathbf{c}}_{a_i} + \bar{\mathbf{t}}_{a_i}^{(n)}), \quad \text{where } \bar{\mathbf{R}}_{a_i}^{(n)}, \bar{\mathbf{t}}_{a_i}^{(n)} = \text{MLP}^{\mathcal{A}}([\bar{\mathbf{f}}_{a_i}, \mathbf{z}^{(n)}]; W^{\mathcal{A}}), \quad (4)$$

where $[\cdot, \cdot]$ denotes concatenation, and the MLP with weights $W^{\mathcal{A}}$ returns a rotation $\bar{\mathbf{R}}_{a_i}^{(n)} \in SO(3)$ and translation vector $\bar{\mathbf{t}}_{a_i}^{(n)} \in \mathbb{R}^3$. To capture fine-scale flexibility, additional shifts are applied to individual Gaussians (Fig. 2C, middle), i.e.,

$$\mathbf{c}_i^{(n)} = \tilde{\mathbf{c}}_i^{(n)} + \mathbf{t}_i^{(n)}, \quad \text{where } \mathbf{t}_i^{(n)} = \text{MLP}_c^{\mathcal{G}}([\mathbf{f}_i, \mathbf{z}^{(n)}]; W_c^{\mathcal{G}}). \quad (5)$$

Here, the network $\text{MLP}_c^{\mathcal{G}}$, with separate weights $W_c^{\mathcal{G}}$, generates individual Gaussian displacements, $\mathbf{t}_i^{(n)} \in \mathbb{R}^3$, which are smooth as Gaussians associated with the same anchor will have similar features.

Finally, to account for compositional variability, where regions of a density map may be missing, we modulate Gaussian amplitudes (Fig. 2C, bottom), as

$$m_i^{(n)} = m_i \times \sigma_i^{(n)}, \quad \text{where } \sigma_i^{(n)} = \text{MLP}_m^{\mathcal{G}}([\mathbf{f}_i, \mathbf{z}^{(n)}]; W_m^{\mathcal{G}}). \quad (6)$$

Here, $\text{MLP}_m^{\mathcal{G}}$ is an MLP with a sigmoid output activation to restrict the modulation to $(0, 1)$. Values close to 0 and 1, respectively, correspond to inactive (absent) and active (present) Gaussians. Considering both modifications to centers and amplitudes, we obtain a modulated set of 3D Gaussians for n -th particle image, $\mathcal{G}^{(n)} = \{(\mathbf{c}_i^{(n)}, s_i, m_i^{(n)})\}$. Gaussian scales remain the same as they control local resolution, a factor independent of structural variability.

We jointly optimize the parameters Θ (which includes Gaussian and anchor parameters and MLP weights), and the per-image latent coordinates, $Z = \{\mathbf{z}^{(n)}\}$, by minimizing the objective (Fig. 2D)

$$L(\Theta, Z) = \frac{1}{N} \sum_{n=1}^N \mathcal{L}(I^{(n)}, \hat{I}^{(n)}) + \lambda_z \|\mathbf{z}^{(n)}\|_2^2 + \lambda_f \sum_{i=1}^G \|\Delta \mathbf{f}_i\|_2^2, \quad (7)$$

where the reconstruction loss, \mathcal{L} , is proportional to the negative image log-likelihood (i.e., the squared error between $I^{(n)}$ and $g^{(n)} \star \hat{I}^{(n)}$ where $g^{(n)}$ is the microscope point spread function and $\hat{I}^{(n)}$ is the 2D projection of $\mathcal{G}^{(n)}$ from Eq. 2). The second term imposes a zero-mean Gaussian prior over the per-image latent codes, ensuring latent coordinates remain bounded [26, 33], while the third term regularizes Gaussians to remain close to the anchor in the feature space. λ_z and λ_f are hyperparameters that control the relative strength of these priors.

3.2 Part Discovery for Model Initialization

The part discovery process is illustrated in Fig. 2A. We optimize a coarse-grained model without anchors and with fewer Gaussians, similarly parameterized as $\mathcal{G} = \{(\mathbf{f}_i, \mathbf{c}_i, s_i, m_i)\}_{i=1}^G$. Here, the Gaussian features, \mathbf{f}_i , are directly learnable parameters (and randomly initialized). We use $\text{MLP}_c^{\mathcal{G}}$ (Eq. 5), to shift Gaussian centers and $\text{MLP}_m^{\mathcal{G}}$ (Eq. 6) to modulate Gaussian amplitudes. The parameters are estimated using the L2 reconstruction loss and the latent prior, similar to the objective in Eq. 7. Once optimized, we find that the feature space naturally groups Gaussians into 3D parts that undergo consistent motion or appear and disappear together. Remarkably, this property emerges without any direct supervision on features.

To obtain parts, we apply clustering on the Gaussian features, thereby finding regions with reasonably consistent motion and presence. We then further divide these clusters by clustering in 3D space to ensure large parts are well-covered with anchors. For clustering we simply use k-means++ [1]. We use the position and feature vector of the Gaussian closest to the centroid of the cluster to initialize the anchor set, $\mathcal{A} = \{(\bar{\mathbf{c}}_a, \bar{\mathbf{f}}_a)\}_{a=1}^A$. From the coarse-grained model, we also compute an improved density map which is used to seed the Gaussians of the part-aware model. This provides a more robust initialization, especially in the presence of large-scale motion which can lead to blurred or over-dispersed density. Lastly, the coarse-grained model provides a preliminary estimate of the image latent codes, which are used to initialize latent codes in the part-aware model.

Remark. Methods for 4D scene reconstruction [27, 31], and DynaMight [40] in cryo-EM, often use neural networks to output deformations or motion. However, they condition on positional encodings of input coordinates instead of learnable features. Such fixed conditioning strongly biases deformations to be spatially smooth, whereas our approach with learnable feature space enables a more flexible form of piecewise smoothness, allowing nearby parts to move quite differently. Through an ablation study, we show that positional encodings quantitatively underperform as well.

4 Experimental Setup

We quantitatively compare CryoSPIRE with the state-of-the-art methods, namely, RECOVER [10], CryoDRGN [47], DRGN-AI [19], 3DFlex [33] and 3DVA [32] using the CryoBench benchmark [15]. We also provide qualitative results on experimental datasets.

CryoBench. The sole benchmark for cryo-EM heterogeneity is CryoBench [15], a set of synthetic datasets with ground-truth labels and a protocol for quantitative evaluation. Two datasets, *IgG-ID* and *IgG-RL*, are based on the human immunoglobulin G (IgG) complex, simulating conformational changes by rotating the dihedral angle between the Fab domain and the IgG core (see Fig. 4D), generating 100 distinct conformations, each with 1,000 particle images. *Ribosembly* simulates compositional heterogeneity by successively adding protein subunits and ribosomal RNA, resulting in 16 discrete structural states [35]. It has 335,240 particle images, with non-uniform distribution over the 16 compositional states. All particle images have 128×128 pixels, and are simulated with realistic point spread functions and a signal-to-noise ratio (SNR) of 0.01.

Experimental Datasets. We also evaluate on two real datasets: EMPIAR-10076 is a dataset comprising assemblies of intermediates of the *Escherichia coli* large ribosomal subunit (LSU) [7], with 131,899 particle images (320×320 pixels, with pixel size 1.31 Å). In the original study, four major assembly states were identified [7], with a subset of particles labeled as unassigned (non-ribosomal impurities) or 30S subunits. We also consider EMPIAR-10180, a conformationally heterogeneous dataset of Pre-Catalytic Spliceosome [30]. A total of 327,490 particle images were collected (320×320 pixels, with pixel size 1.69 Å). Consistent with other heterogeneity methods considering this dataset [10, 47] we perform analysis on a filtered subset of 139,722 images.

Implementation Details. For part discovery, we seed $G = 2,048$ components using the rigid reconstruction and adopt lightweight MLPs with a single hidden layer of $H = 32$ units. The latent space, \mathcal{Z} , has dimensionality $D = 4$ and the feature space, \mathcal{F} , has dimensionality $E = 24$. We optimize

Method	IgG-1D		IgG-RL		Ribosembly	
	Mean (std)	Med	Mean (std)	Med	Mean (std)	Med
3D Classification [39]	0.297 (0.019)	0.291	0.309 (0.01)	0.307	0.289 (0.081)	0.288
CryoDRGN [47]	0.366 (0.003)	0.366	0.349 (0.008)	0.348	0.415 (0.019)	0.415
CryoDRGN-AI-fixed [19]	0.366 (0.001)	0.366	0.355 (0.007)	0.354	0.372 (0.032)	0.374
3DFlex [33]	0.336 (0.002)	0.336	0.339 (0.007)	0.339	-	-
3DVA [32]	0.351 (0.003)	0.351	0.341 (0.006)	0.341	0.375 (0.038)	0.372
RECOVAR [10]	0.391 (0.001)	0.391	0.372 (0.008)	0.371	0.430 (0.016)	0.432
CryoSPIRE (ours)	0.402 (0.002)	0.402	0.386 (0.014)	0.389	0.427 (0.014)	0.424

Table 1: Mean (standard deviation) and median of AUC of Per-Conformation FSCs on CryoBench datasets [15]. Statistics computed across different structural states, i.e. 100 for IgG-1D and IgG-RL and 16 for Ribosembly (Best method in bold, second best underlined).

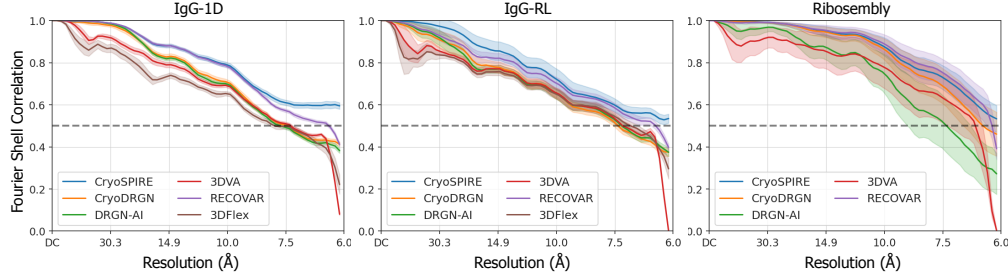


Figure 3: Per-Conformation FSC on CryoBench datasets. Error bars indicate standard deviation across different conformations. The highest possible resolution is 6 Å on these synthetic datasets.

the part discovery model for 15 and 50 epochs on synthetic and experimental datasets. The part-aware GMMs are optimized for 30 epochs, using $G=8,192$ components, except for Ribosome synthetic and experimental datasets with $G=16,384$, and have MLPs with three hidden layers and $H=128$ hidden units. On experimental datasets, we perform part discovery on downsampled 128×128 images for efficiency, while the part-aware GMM is optimized on 256×256 images. We use batch size $B=64$ and set hyperparameters $\lambda_z = 0.1$, $\lambda_f = 0.01$. The optimization runs on a single NVIDIA GeForce RTX 2080, taking 3 to 6 hours depending on the number of Gaussians in the model.

Evaluation Metrics. The quality of cryo-EM density maps are evaluated using Fourier Shell Correlation (FSC) [43], which is the normalized cross-correlation between two independently estimated density maps, as a function of frequency. Metrics for heterogeneity are less standardized, but the most common is Per-Conformation FSC (or Per-Conf FSC) [15], proposed by CryoBench [15]. Per-Conf FSC is the average FSC between the ground-truth 3D structure of a particle state, and the 3D structure corresponding to the average latent position of images associated with that state. The Per-Conf FSC requires knowledge of ground-truth 3D structures for each image which is not available for experimental data and we instead rely on qualitative evaluation of the estimated parts and structures. FSC results in a curve which can be summarized by computing the area under the curve (AUC) to more easily compare methods. See the supplement for more details on metrics.

5 Results

Quantitative comparison on the three relevant CryoBench [15] datasets are provided in Table 1 and Fig. 3. Note that CryoSPIRE outperforms 3DVA and 3DFlex which are among the most widely used methods in cryo-EM at present. As 3DFlex cannot handle compositional changes, it was not evaluated on Ribosembly. CryoSPIRE outperforms non-linear latent variable models, Cryo-DRGN and DRGN-AI, especially on IgG-1D and IgG-RL by a large margin. The most competitive method is the linear subspace model of RECOVAR, which, as reported, is memory intensive due to allocation of several bases and is not as interpretable without motion modeling. While CryoSPIRE significantly outperforms RECOVAR on IgG datasets, its performance on Ribosembly, where linear subspace models are more favorable by design, is not statistically different from RECOVAR. Relative to the nominal FSC threshold of 0.5 for comparison to ground truth [36], the FSC curves in Fig. 3 indicate that CryoSPIRE finds higher resolution density maps. Finally, we note that CryoSPIRE is the first GMM-based method to be successfully evaluated on CryoBench.

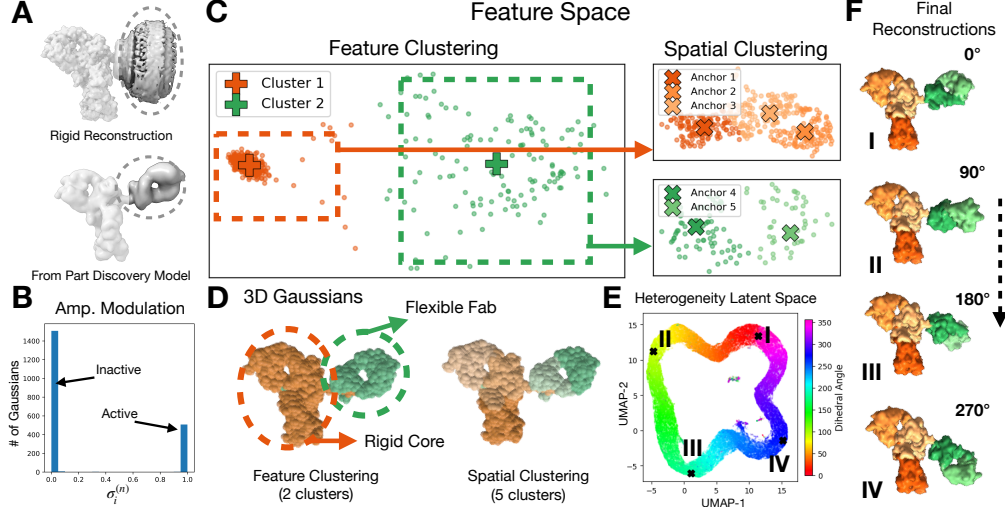


Figure 4: Results on IgG-1D [15]. (A) Due to large motion, the Fab domain (circled) is smeared out in rigid reconstruction, while our part discovery model identifies this domain and resolves its structure and motion, providing good initialization for subsequent modeling. (B) For a sample structure, the histogram of amplitude modulations indicate active and inactive Gaussians. (C) Gaussian feature space, \mathfrak{F} , shows two distinct groups (green, orange), corresponding to the flexible Fab and the rigid core; feature clustering finds these groups and divides further based on spatial proximity, yielding 5 parts. (D) Configuration of 3D Gaussians after Level-1 and Level-2 clustering. (E) The latent space, \mathfrak{Z} , captures conformation change (colored based on ground truth Fab orientation). (F) Sample structures from model corresponding to four latent points, showing rotation of the Fab domain (green).

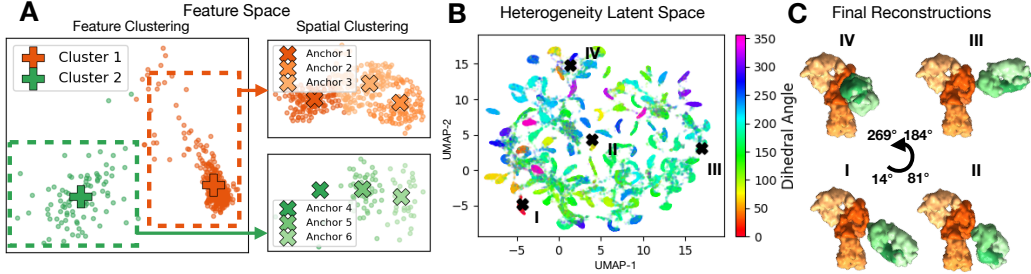


Figure 5: Results on IgG-RL [15]. (A) The feature space, \mathfrak{F} , shows two parts (green and orange) corresponding to the flexible Fab domain and the rigid core. Subsequent spatial clustering yields six parts. (B) The latent space, \mathfrak{Z} , is colored with Fab orientation along with four sampled latent points that capture rotation of the Fab domain (comprising three parts). The motion of the Fab domain in IgG-RL is not as regular as that in IgG-1D, as reflected in the latent space. (C) The corresponding density maps are provided with parts illustrated in different colors.

IgG-1D & IgG-RL (CryoBench [15]). The flexible Fab domain (circled in Fig. 4A, top) in the rigid reconstruction, used as input for part discovery, is poorly resolved. However, the part discovery model learns to selectively deactivate incoherent parts, as shown in the histogram of the modulation factors $\sigma_i^{(n)}$ in Fig. 4B. This enables a more robust initialization (Fig. 4A, bottom) of the hierarchical GMM. The Gaussian feature space, \mathfrak{F} , shows two clusters corresponding to the flexible Fab domain from the rigid core (Fig. 4C for IgG-1D and Fig. 5B for IgG-RL). Spatial clustering produces a total of five and six anchors for IgG-1D and IgG-RL, respectively. The latent heterogeneity space, \mathfrak{Z} , indicates a circular manifold of dihedral angles for IgG-1D, see Fig. 4D. Four structures from the latent space in both datasets demonstrate that the Fab domain, covered by a few parts, undergo a large, predominantly rigid motion, while the rest of the complex is remains fixed.

Ribosembyl (CryoBench [15]). After part discovery, we obtain eight parts (see Fig. 6A) that are used to initialize eight anchors in the part-aware GMM. In Fig. 6B the learned latent space, \mathfrak{Z} , clearly distinguishes between the different compositional states. For seven selected states, we visualize the estimated structure (Fig. 6C), colored based on the discovered parts.

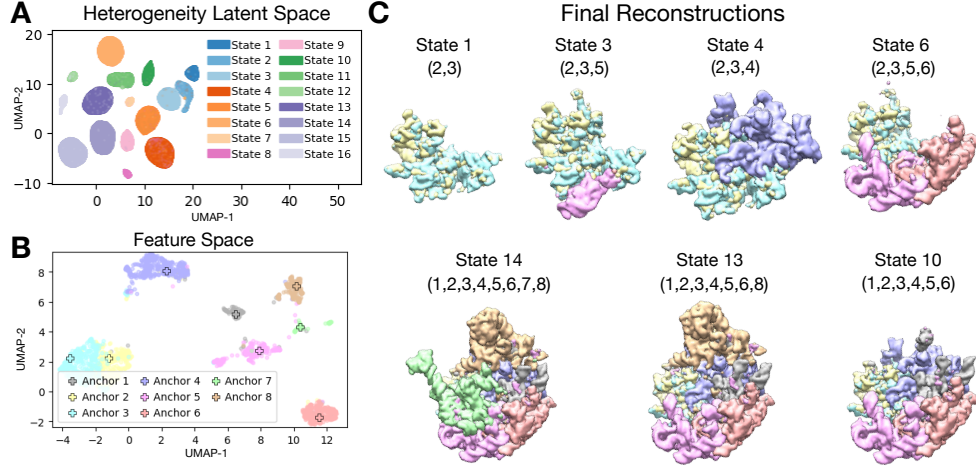


Figure 6: Results on Ribosemblly [15] (A) Gaussian feature space, \mathfrak{F} , showing eight major parts identified through clustering. (B) Heterogeneity latent space, \mathfrak{Z} , colored coded with the ground-truth compositional state. (C) Visualizations of 3D density maps corresponding to seven points in latent space, with colors depicting parts (given in parentheses).

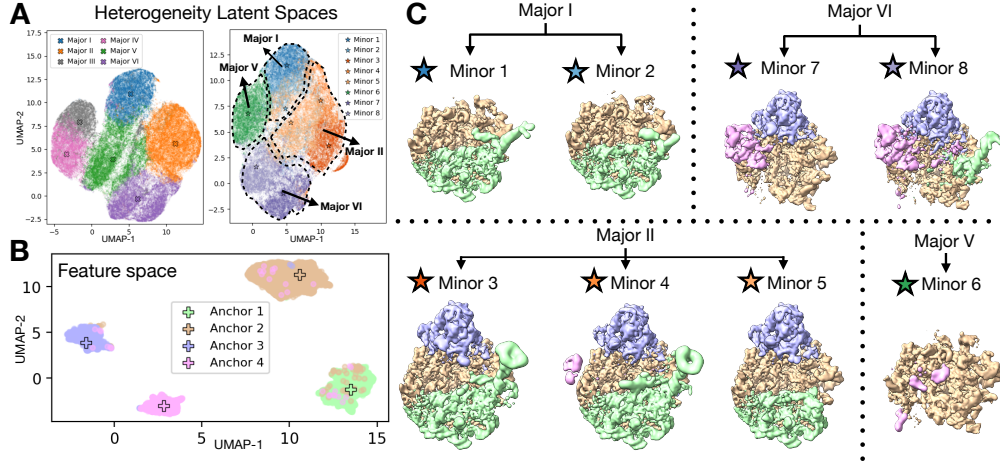


Figure 7: Results on Large Ribosomal Subunit (EMPIAR-10076 [7]). (A) The learned heterogeneity latent spaces, \mathfrak{Z} , in part discovery (left) identifies the four major assembly states (I, II, V, VI) and two groups of impurities (III, IV). After fitting the part-aware model, the major states, with impurities excluded, can be further categorized (right) into eight color-coded minor structural states. (B) The part discovery Gaussian feature space, \mathfrak{F} , reveals four parts which are used to construct the part-aware model. (C) The structures corresponding to different states, colored by inferred part.

Large Ribosomal Subunit (EMPIAR-10076 [7]). We find four major assembly states in the part discovery latent space (labeled as (I, II, V, VI) in Fig. 7A, left), which match classes (C, E, B, D) in the original study [7], with unassigned particles and 30S contaminants grouped in states III and IV, which are excluded when optimizing hierarchical model (See supplement for more details). The Gaussian feature space, \mathfrak{F} , (Fig. 7B) shows four distinct parts which also align with previously reported structural blocks in the original study (cf. [7], Fig. 6). By analyzing the heterogeneity latent space, \mathfrak{Z} , of the part-aware model (Fig. 7A, right), we show that the major states can be further divided into subpopulations; e.g., the major state I is represented with minor states (1, 2) and the major state II has branched into minor states (3, 4, 5). The associated structures, shown in Fig. 7E, are consistent with minor states reported in the original study [7].

Pre-Catalytic Spliceosome (EMPIAR-10180 [30]). The feature space, \mathfrak{F} , of the part discovery model (Fig. 8B), shows four distinct clusters, which correspond to coherent structural regions – foot, body, helicase, and SF3b – consistent with the original study [30]. Accordingly, we optimize

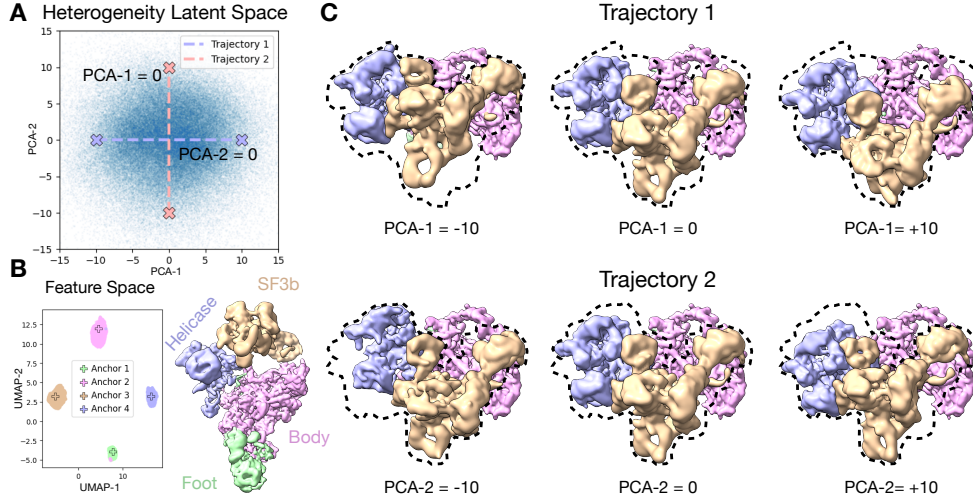


Figure 8: Results on Pre-Catalytic Spliceosome (EMPIAR-10180 [30]). (A) PCA of the latent space, \mathcal{Z} , is used to generate two structural trajectories. (B) The Gaussian feature space, \mathcal{F} , shows four parts which correspond to known helicase, SF3b, body and foot domains as shown in 3D visualization of Gaussian components configuration. (C) Three states along each trajectory. In both trajectories, body is rigid while SF3b and helicase show large-scale motion.

Method	IgG-1D	IgG-RL	Ribosembly
CryoSPIRE	0.402 (0.002)	0.386 (0.014)	0.427 (0.014)
w/o hier. motion	0.388 (0.002)	0.372 (0.010)	0.425 (0.015)
over-segment	0.384 (0.002)	0.375 (0.010)	0.423 (0.016)
w/ pos. encoding	0.377 (0.002)	0.361 (0.007)	0.415 (0.023)

Table 2: Mean AUC-FSCs reported on datasets from CryoBench [15] for ablation study.

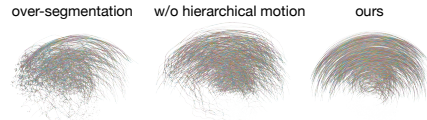


Figure 9: Estimated motion of Gaussians for 30 states of IgG-1D. The baselines fail to capture local rigidity.

the part-aware model with four anchors. To illustrate structural variability, we run PCA on the heterogeneity latent space, \mathcal{Z} , and extract two principal directions illustrated in Fig. 8A. Top views of density maps along the two principal directions (Fig. 8C) show two modes of conformational heterogeneity. The first direction reflects a forward-backward rotation of the SF3b and helicase regions. The second direction captures a side-to-side rotation of SF3b, and a diagonal shift of the helicase. Please see the supplement for more visualization on conformational changes.

5.1 Ablation Study

Here, we ablate key design decisions in our framework. To demonstrate the importance of anchor-based motion modeling in CryoSPIRE, we consider a baseline without anchors that uses an MLP to directly learn deformations of individual Gaussians. Quantitative comparison on IgG-1D and IgG-RL, as in Table 1, shows that the lack of anchor based motion leads to inferior results. This is less critical for Ribosembly with minor conformational changes. We also compare with a model that over-segments the structure by using $K = 64$ anchors, which achieves worse performance. In Fig. 9, we visualize the estimated motion of Gaussians on the IgG-1D dataset. Both baselines fail to capture the locally rigid and smooth motion. Finally, we consider a baseline where the Gaussian feature space is replaced with a positional encoding, similar to previous methods, e.g., [40]. This baseline is unable to identify meaningful parts and achieves inferior quantitative performance.

6 Conclusion

We present CryoSPIRE, a hierarchical cryo-EM density model to capture conformational and compositional heterogeneity in the 3D structure of biomolecules from 2D images. This includes a novel method for part discovery and a hierarchical Gaussian mixture model for which the parts provide meaningful inductive biases to regularize model fitting. CryoSPIRE establishes a new state-of-the-art on the CryoBench heterogeneous benchmark, and produces meaningful parts on experimental data.

While CryoSPIRE shows promising results, limitations exist. Validation of estimated structures and variability from heterogeneous experimental data remains an open problem for all methods, including CryoSPIRE. Interpreting the inferred latent space remains challenging, specifically how it may relate to the biophysical energy landscape of molecular states. Finally, like other methods, we presume an initial estimate of the structure and image poses; inaccuracies in these may limit CryoSPIRE’s efficacy. A fully *ab initio* method for heterogeneous data remains future work.

Broader Impact

Cryo-electron microscopy (cryo-EM) has emerged as a revolutionary technique in structural biology, enabling the determination of macromolecular structures with significant societal impact. Computational methods, grounded in machine learning and computer vision have now been used to determine many thousands of biological structures. Notably, cryo-EM played a pivotal role in elucidating the structure of the SARS-CoV-2 spike protein, revealing its pre-fusion conformation and aiding in the assessment of medical countermeasures. Complementing computational methods such as AlphaFold for protein structure prediction, cryo-EM has revolutionized our understanding of cellular processes and accelerated the development of novel therapeutics, including synthetic antibodies. Nevertheless, we strongly condemn any usage of our proposed hierarchical 3D GMM representation for generating malicious data, improperly modifying signals, or spreading misinformation.

Acknowledgments and Disclosure of Funding

This research was supported in part by the Province of Ontario, the Government of Canada, through NSERC, CIFAR, and the Canada First Research Excellence Fund for the Vision: Science to Applications (VISTA) programme, and by companies sponsoring the Vector Institute.

References

- [1] David Arthur and Sergei Vassilvitskii. K-Means++: The advantages of careful seeding. *Proc. 18th Annual ACM-SIAM Symposium on Discrete Algorithms*, page 1027–1035, 2007. [5](#), [15](#)
- [2] Jeongmin Bae, Seoha Kim, Youngsik Yun, Hahyun Lee, Gun Bang, and Youngjung Uh. Per-Gaussian embedding-based deformation for deformable 3d Gaussian splatting. In *European Conference on Computer Vision (ECCV)*, pages 321–335. Springer, 2024. [1](#), [3](#)
- [3] Marcus A Brubaker, Ali Punjani, and David J Fleet. Building proteins in a day: Efficient 3d molecular reconstruction. *Proc IEEE Conf. Computer Vision and Pattern Recognition (CVPR)*, 2015. [1](#)
- [4] Muyuan Chen and Steven J Ludtke. Deep learning-based mixed-dimensional Gaussian mixture model for characterizing variability in cryo-EM. *Nature Methods*, 18(8):930–936, 2021. [2](#), [3](#)
- [5] Muyuan Chen, Michael F. Schmid, and Wah Chiu. Improving resolution and resolvability of single particle cryoem structures using Gaussian mixture models. *Nature Methods*, 21:37–40, 2023. [2](#), [3](#)
- [6] Muyuan Chen, Bogdan Toader, and Lederman Roy. Integrating molecular models into cryoem heterogeneity analysis using scalable high-resolution deep Gaussian mixture models. *Journal of Molecular Biology*, 435(9):168014, 2023. [2](#), [3](#), [15](#)
- [7] Joseph H Davis, Yong Zi Tan, Bridget Carragher, Clinton S Potter, Dmitry Lyumkis, and James R Williamson. Modular assembly of the bacterial large ribosomal subunit. *Cell*, 167(6):1610–1622, 2016. [5](#), [8](#), [15](#), [20](#)
- [8] Robert A Drebin, Loren Carpenter, and Pat Hanrahan. Volume rendering. *ACM SIGGRAPH*, 22(4):65–74, 1988. [3](#)
- [9] J. Frank and L. Al-Ali. Signal-to-noise ratio of electron micrographs obtained by cross correlation. *Nature*, 256(5516):376–379, 1975. [16](#)

- [10] Marc Aurèle Gilles and Amit Singer. Cryo-EM heterogeneity analysis using regularized covariance estimation and kernel regression. *Proc. National Academy of Science*, 122(9):e2419140122, 2025. 1, 2, 5, 6, 17
- [11] Antoine Guédon and Vincent Lepetit. Sugar: Surface-aligned Gaussian splatting for efficient 3D mesh reconstruction and high-quality mesh rendering. In *Proc. CVPR*, 2024. 3
- [12] G. Harauz and M. van Heel. Optimal determination of particle orientation, absolute hand, and contrast loss in single-particle electron cryomicroscopy. *Optik*, 73:146–156, 1986. 16
- [13] David Herreros, Roy R Lederman, James M Krieger, Amaya Jiménez-Moreno, Marta Martínez, David Myška, D Strelak, J Filipovic, Carlos OS Sorzano, and José M Carazo. Estimating conformational landscapes from cryo-em particles by 3d zernike polynomials. *Nature Communications*, 14(1):154, 2023. 1
- [14] Yue Huang, Chengguang Zhu, Xiaokang Yang, and Manhua Liu. High-resolution real-space reconstruction of cryo-em structures using a neural field network. *Nature Machine Intelligence*, 6:892–903, 2024. 2
- [15] Minkyu Jeon, Rishwanth Raghu, Miro Astore, Geoffrey Woollard, Ryan Feathers, Alkin Kaz, Sonya M. Hanson, Pilar Cossio, and Ellen D. Zhong. CryoBench: Diverse and challenging datasets for the heterogeneity problem in cryo-em. In *Advances in Neural Information Processing Systems (NeurIPS)*, 2024. 2, 5, 6, 7, 8, 9, 15, 16, 17, 18, 19
- [16] Bernhard Kerbl, Georgios Kopanas, Thomas Leimkuehler, and George Drettakis. 3D Gaussian splatting for real-time radiance field rendering. *ACM Transactions on Graphics (Proc. SIGGRAPH)*, 2023. 3, 15
- [17] Shakiba Kheradmand, Daniel Rebain, Gopal Sharma, Weiwei Sun, Yang-Che Tseng, Hossam Isack, Abhishek Kar, Andrea Tagliasacchi, and Kwang Moo Yi. 3D Gaussian splatting as Markov chain Monte Carlo. In *Proc. NeurIPS*, 2024. 3
- [18] Werner Kühlbrandt. The Resolution Revolution: Advances in detector technology and image processing are yielding high-resolution electron cryo-microscopy structures of biomolecules. *Science*, 343(6178):1443–1444, 2014. 1
- [19] Axel Levy, Michal Grzadkowski, Frederic Poitevin, Francesca Vallese, Oliver B Clarke, Gordon Wetzstein, and Ellen D Zhong. Revealing biomolecular structure and motion with neural ab initio cryo-em reconstruction. *bioRxiv*, 2024. 1, 2, 5, 6, 17, 19
- [20] Axel Levy, Gordon Wetzstein, Julien NP Martel, Frederic Poitevin, and Ellen Zhong. Amortized inference for heterogeneous reconstruction in cryo-EM. *Advances in Neural Information Processing Systems*, 35:13038–13049, 2022. 1
- [21] Tao Lu, Mulin Yu, Linning Xu, Yuanbo Xiangli, Limin Wang, Dahua Lin, and Bo Dai. Scaffoldgs: Structured 3d Gaussians for view-adaptive rendering. In *Proc IEEE/CVF Conf Computer Vision and Pattern Recognition (CVPR)*, pages 20654–20664, 2024. 2, 3
- [22] Jonathon Luiten, Georgios Kopanas, Bastian Leibe, and Deva Ramanan. Dynamic 3D Gaussians: Tracking by persistent dynamic view synthesis. In *Proc. 3DV*, 2024. 3
- [23] Nelson Max. Optical models for direct volume rendering. *IEEE Trans. Vis. Comput. Graph.*, 1(2):99–108, 2002. 3
- [24] Ben Mildenhall, Pratul P Srinivasan, Matthew Tancik, Jonathan T Barron, Ravi Ramamoorthi, and Ren Ng. NERF: Representing scenes as neural radiance fields for view synthesis. *Communications of the ACM*, 65(1):99–106, 2022. 2
- [25] Takanori Nakane and Sjors HW Scheres. Multi-body refinement of cryo-em images in relion. In *CryoEM: Methods and Protocols*, pages 145–160. Springer, 2020. 3
- [26] Jeong Joon Park, Peter Florence, Julian Straub, Richard Newcombe, and Steven Lovegrove. DeepSDF: Learning continuous signed distance functions for shape representation. In *Proc IEEE/CVF Conf Computer Vision and Pattern Recognition (CVPR)*, pages 165–174, 2019. 5

- [27] Keunhong Park, Utkarsh Sinha, Jonathan T Barron, Sofien Bouaziz, Dan B Goldman, Steven M Seitz, and Ricardo Martin-Brualla. Nerfies: Deformable neural radiance fields. In *Proc IEEE/CVF International Conference on Computer Vision (CVPR)*, pages 5865–5874, 2021. 5
- [28] Pawel A. Penczek. Three-dimensional spectral signal-to-noise ratio for a class of reconstruction algorithms. *Journal of Structural Biology*, 138(1):34–46, 2002. 16
- [29] Eric F Pettersen, Thomas D Goddard, Conrad C Huang, Elaine C Meng, Gregory S Couch, Tristan I Croll, John H Morris, and Thomas E Ferrin. Ucsf chimeraX: Structure visualization for researchers, educators, and developers. *Protein science*, 30(1):70–82, 2021. 14
- [30] Clemens Plaschka, Pei-Chun Lin, and Kiyoshi Nagai. Structure of a pre-catalytic spliceosome. *Nature*, 546(7660):617–621, 2017. 5, 8, 9, 15, 20, 21
- [31] Albert Pumarola, Enric Corona, Gerard Pons-Moll, and Francesc Moreno-Noguer. D-nerf: Neural radiance fields for dynamic scenes. In *Proc IEEE/CVF Conf on Computer Vision and Pattern Recognition (CVPR)*, pages 10318–10327, 2021. 5
- [32] Ali Punjani and David J Fleet. 3D Variability Analysis: Directly resolving continuous flexibility and discrete heterogeneity from single particle cryo-EM images. *Journal of Structural Biology*, 213:107702, 2021. 1, 2, 5, 6, 17, 19, 20, 21
- [33] Ali Punjani and David J Fleet. 3DFlex: Determining structure and motion of flexible proteins from cryo-em. *Nature Methods*, 20:860–870, 2023. 1, 2, 3, 5, 6, 17, 19, 20, 21
- [34] Ali Punjani, John L Rubinstein, David J Fleet, and Marcus A Brubaker. CryoSPARC: Algorithms for rapid unsupervised cryo-em structure determination. *Nature Methods*, 14:290–296, 2017. 15, 20
- [35] Bo Qin, Simon M Lauer, Annika Balke, Carlos H Vieira-Vieira, Jörg Bürger, Thorsten Mielke, Matthias Selbach, Patrick Scheerer, Christian MT Spahn, and Rainer Nikolay. Cryo-em captures early ribosome assembly in action. *Nature Communications*, 14(1):898, 2023. 5
- [36] P. B. Rosenthal and R. Henderson. Optimal determination of particle orientation, absolute hand, and contrast loss in single-particle electron cryomicroscopy. *J. Molecular Biology*, 333(4):721–745, 2003. 6, 16
- [37] Sjors H. W. Scheres. RELION: Implementation of a Bayesian approach to cryo-em structure determination. *Journal of Structural Biology*, 180(3):519 – 530, 2012. 15
- [38] Sjors H W Scheres. Processing of structurally heterogeneous cryo-em data in RELION. In R A Crowther, editor, *The Resolution Revolution: Recent Advances In cryoEM*, volume 579 of *Methods in Enzymology*, pages 125–157. Academic Press, 2016. 1
- [39] Sjors H W Scheres, Haixiao Gao, Mikel Valle, Gabor T Herman, Paul P B Eggermont, Joachim Frank, and Jose-Maria Carazo. Disentangling conformational states of macromolecules in 3D-EM through likelihood optimization. *Nature Methods*, 4(1):27–29, 2007. 6, 17
- [40] Johannes Schwab, Dari Kimanius, Alister Burt, Tom Dendooven, and Sjors H. W. Scheres. DynaMight: Estimating molecular motions with improved reconstruction from cryo-em images. *Nature Methods*, 21:1855–1862, 2024. 2, 3, 5, 9
- [41] Amit Singer and Fred J Sigworth. Computational methods for single-particle electron cryomicroscopy. *Annual review of biomedical data science*, 3(1):163–190, 2020. 14
- [42] M. Unser, B. L. Trus, and A. C. Steven. A new resolution criterion based on spectral signal-to-noise ratios. *Ultramicroscopy*, 23(1):39–51, 1987. 16
- [43] Marin Van Heel and Michael Schatz. Fourier shell correlation threshold criteria. *Journal of structural biology*, 151(3):250–262, 2005. 6, 16
- [44] Guanjun Wu, Taoran Yi, Jiemin Fang, Lingxi Xie, Xiaopeng Zhang, Wei Wei, Wenyu Liu, Qi Tian, and Xinggang Wang. 4D Gaussian splatting for real-time dynamic scene rendering. In *Proc. CVPR*, 2024. 3

- [45] Ziyi Yang, Xinyu Gao, Wen Zhou, Shaohui Jiao, Yuqing Zhang, and Xiaogang Jin. Deformable 3D Gaussians for high-fidelity monocular dynamic scene reconstruction. In *Proc. CVPR*, 2024. 3
- [46] Zehao Yu, Anpei Chen, Binbin Huang, Torsten Sattler, and Andreas Geiger. Mip-splatting: Alias-free 3D Gaussian splatting. In *Proc. CVPR*, 2024. 3
- [47] Ellen D. Zhong, Tristan Bepler, Bonnie Berger, and Joseph H. Davis. CryoDRGN: Reconstruction of heterogeneous cryo-em structures using neural networks. *Nature Methods*, 18:176–185, 2021. 1, 2, 5, 6, 17, 19, 20, 21
- [48] Matthias Zwicker, Hanspeter Pfister, Jeroen Van Baar, and Markus Gross. Ewa splatting. *IEEE Transactions on Visualization and Computer Graphics*, 8(3):223–238, 2002. 3

Supplementary Material

Reconstructing Heterogeneous Biomolecules via Hierarchical Gaussian Mixtures and Part Discovery

A Project Webpage

We share a [Project Webpage](#), presenting short videos describing CryoSPIRE and showing qualitative comparisons with baseline methods on synthetic and experimental data. We use ChimeraX [29] to create detailed 3D visualizations of reconstructions shown in Figs. 12, 13, and 14. In the webpage, we also demonstrate how navigating the learned latent space leads to various structural states reconstructed by CryoSPIRE.

B GMM Image Formation, Parameterization and Rendering

In cryo-EM, the image formation process follows integral projection of a 3D density to the 2D image plane. For a 3D Gaussian mixture, the projection is analytically tractable, as described in Sec. 2, Eq. 2. For the purposes of optimization, however, we adopt a slightly different parameterization as we find it to be somewhat better behaved. Assuming each 3D Gaussian component in the mixture is parameterized with center $\mathbf{c} \in \mathbb{R}^3$, isotropic scale $s \in \mathbb{R}$, and an amplitude $m \in \mathbb{R}$, we define the 2D noise-free projection along the canonical z -axis, for location $\tilde{\mathbf{p}} \in \mathbb{R}^2$, as

$$\tilde{I}(\tilde{\mathbf{p}}) = \sum_i m_i \exp\left(-\frac{\|\tilde{\mathbf{p}} - [\mathbf{c}_i]_{xy}\|_2^2}{2s_i^2}\right) \quad (8)$$

Here, we modify the weight of terms such that the peak intensity of each Gaussian term solely depends on the amplitudes m_i , whereas, in Eq. 2, it is proportional to both s_i and m_i . This leads to a direction of ambiguity in the optimization landscape where increasing one parameter (e.g. m_i) and decreasing the other (e.g. s_i) can compensate; the coupling between m_i and s_i makes it challenging to set learning rates and it destabilizes the optimization dynamics. The alternative parameterization in Eq. 8 that we use is mathematically equivalent to the following weighting of the 3D mixture:

$$f(\mathbf{p}) = \sum_i \frac{m_i}{\sqrt{2\pi}s_i} \exp\left(-\frac{\|\mathbf{p} - \mathbf{c}_i\|_2^2}{2s_i^2}\right), \quad (9)$$

for location $\mathbf{p} \in \mathbb{R}^3$. This simply involves a change of variables, i.e., $m_i \rightarrow m_i/\sqrt{2\pi}s_i$.

As discussed in the introduction of the paper, cryo-EM images are extremely noisy, since low electron dosages are used to minimize radiation damage to the particles. To ensure sufficient image contrast, the microscope is defocused, which is modeled as convolution with a image-specific point-spread function (PSF), $g^{(n)}$, or, more commonly as modulation in the Fourier domain with a contrast transfer function (CTF) [41]. Finally, we model all sources of noise with additive, zero-mean Gaussian noise, $\epsilon^{(n)} \sim \mathcal{N}(\mathbf{0}, \sigma^2 I)$. Taken together, the final image can be expressed as,

$$\hat{I}^{(n)} = g^{(n)} \star \tilde{I}^{(n)} + \epsilon^{(n)} \quad (10)$$

For optimization, we minimize a squared L2 reconstruction loss between model predictions and observed image, which is proportional to the negative log-likelihood,

$$\mathcal{L}(I^{(n)}, \hat{I}^{(n)}) = \|I^{(n)} - \hat{I}^{(n)}\|_2^2. \quad (11)$$

Implementation. Among the Gaussian parameters, the scale is constrained to be positive, and amplitudes are constrained to be non-negative. The centers have no hard constraints. To realize such constraints, we define s_i in the log-scale domain, $s_i = \exp(\tilde{s}_i)$. We also use a ReLU activation function to ensure that amplitudes are non-negative, i.e., $m_i = \text{ReLU}(\tilde{m}_i)$. Thus, the free parameters are $\{(\mathbf{c}_i, \tilde{s}_i, \tilde{m}_i)\}_i$.

The rendering equation (Eq. 8) defines a function I on the 2D plane. We discretize the function within a box $[-0.5, 0.5]^2$ using a regular $L \times L$ grid, denoted $\Lambda = \{(x_u, y_v)\}_{u,v=1}^L$. A naive way to

evaluate I on is to compute the contribution of Gaussian terms separately per-point on the grid, which can be stored collectively in a $G \times L \times L$ matrix. Following [6], we can simplify that computation since 2D Gaussians can be expressed as a separable product of 1D Gaussians (on rows and columns):

$$\exp\left(-\frac{\|\mathbf{p}_{xy} - \tilde{\mathbf{c}}_{i,xy}\|_2^2}{2s_i^2}\right) = \exp\left(-\frac{\|\mathbf{p}_x - \tilde{\mathbf{c}}_{i,x}\|_2^2}{2s_i^2}\right) \exp\left(-\frac{\|\mathbf{p}_y - \tilde{\mathbf{c}}_{i,y}\|_2^2}{2s_i^2}\right). \quad (12)$$

All points within a single row or column in the grid share corresponding 1D Gaussian terms, which thus need to be computed only once. To this end, we decompose the 2D grid Λ into two 1D grids $\Lambda_x = \{x_u\}_{u=1}^L$ and $\Lambda_y = \{y_v\}_{v=1}^L$, and accordingly compute two $G \times L$ matrices, M_x and M_y ,

$$M_x(i, x_u) = \exp\left(-\frac{\|x_u - \tilde{\mathbf{c}}_{i,x}\|_2^2}{2s_i^2}\right), \quad M_y(i, y_v) = \exp\left(-\frac{\|y_v - \tilde{\mathbf{c}}_{i,y}\|_2^2}{2s_i^2}\right). \quad (13)$$

These matrices store the value of 1D Gaussian terms on 1D grids.

We also define all amplitudes within a $G \times 1$ matrix, denoted as W , with $W_{i,1} = m_i$. Next, we use fast matrix operations on W , M_x and M_y , to realize the above rendering equation (Eq. 8). We first compute vectorized outer product between W and M_x , yielding a new $G \times 1 \times L$ matrix. We then compute vectorized outer product between the resulting matrix and M_y , yielding a final matrix of size $G \times 1 \times L \times L$, followed by reducing the first dimension using summation. As a result, we obtain a $1 \times L \times L$ matrix which is our desired discretized projection. Importantly, compared to the naive process, this approach avoids redundant computations using separability of 2D Gaussians.

C CryoSPIRE Initialization

Before describing the initialization process of the coarse-grained GMM for part discovery, we outline how to obtain a preliminary density map as a rigid reconstruction, as well as per-image poses and CTF parameters. For CryoBench [15] datasets, the ground-truth CTFs and poses are provided for each particle image. Given the poses, we use a simple form of backprojection to compute an initial rigid reconstruction. For Ribosome experimental data [7] (EMPIAR-10076), we estimate per-particle poses and an initial rigid reconstruction using CryoSPARC [34]. For Spliceosome [30] (EMPIAR-10180), an initial rigid reconstruction and per-particle poses are available (computed using RELION [37]). For both experimental datasets, CTFs are estimated in a standard preprocessing stage.

As demonstrated in the Gaussian Splatting literature [16], the optimization dynamics are highly sensitive to the initial values of Gaussian parameters. For the coarse-grained GMM used for part discovery, we use the input rigid reconstruction to seed $G = 2048$ Gaussians. Given the input density map, we discard voxels with density below a user-defined threshold, and then sample G of the remaining voxels with probability proportional to density. Gaussians are then seeded at those positions. Note that, since flexible regions often exhibit lower density in the rigid reconstruction, setting the threshold too high may exclude these regions, resulting in poor initialization. Finally, we initialize the amplitude and scales to user-defined values, $m_i = 0.15$, $s_i = 0.02$.

To initialize the hierarchical model, we need to determine the anchors. We run k-means++ [1] clustering on the learned Gaussian features from the part discovery model. UMAP visualizations (Figs. 4, 5, 6, 7, 8) indicate that the feature space contains well-separated clusters of Gaussian components. This clear distinction between clusters provide the potential to automatically set the number of anchors, yet for now we choose number of anchors manually (eg with UMAP visualization). Each anchor receives a feature vector that is set to the centroid of its features in the cluster, and its position is set to that of the closest Gaussian component in the feature space. Feature-based clustering is followed by spatial clustering for IgG data to further divide clusters into local regions, improving coverage of the density map. Furthermore, the part discovery model provides an improved density map, where amplitude modulation helps to identify unused components that can be discarded. Based on this density map, we follow a similar procedure to seed a denser set of Gaussian components. Each new Gaussian is connected to the anchor that the closest Gaussian in the part discovery model is assigned to. Feature offsets are initialized to zero, so Gaussians initially inherit the features of their anchors. We initialize amplitudes as $m_i = 0.15$. But we use lower initial scale values $s_i = 0.01$, since this initialization uses a high quality, more reliable density map.

D FSC-based Performance Metrics

Evaluation of cryo-EM methods is very challenging, in part because ground truth 3D density maps do not exist for experimental data. To date, the most widely used metric, namely, Fourier Shell Correlation (or FSC), is a measure of consistency, defined as the normalized cross-correlation of two 3D density maps computed as a function of frequency [12, 43]. Given two 3D density maps A and B with Fourier coefficients A_j and B_j , the FSC at wavelength λ is defined as

$$\mathcal{F}_\lambda = \frac{\sum_{j \in S_\lambda} A_j B_j^*}{\sqrt{\sum_{j \in S_\lambda} |A_j|^2 \sum_{j \in S_\lambda} |B_j|^2}}, \quad (14)$$

where S_λ is the set of Fourier indices for frequencies within a spherical shell with wavelength λ centered at the origin. Here, $|z|$ is the modulus of the complex scalar z , and z^* is the complex conjugate of z .

FSC can measure consistency between an estimated density map and a ground truth map. Signal-to-noise ratios in particle images, and hence in 3D reconstructions will decrease with frequency. So FSC is usually close to 1 at low frequencies, and then decrease toward zero at higher frequencies where observations are missing or dominated by noise. As a consequence, there are two common ways to characterize the quality of 3D reconstructions. One is the area-under-the-curve (AUC) of the FSC curve. The other is a resolution of the map, defined as the wavelength at which FSC drops below a threshold. A threshold of 0.5 is used for FSC computed between an estimated map and a ground truth map [36], which corresponds to a SNR of 1 (an estimator of spectral SNR from FSC is simply $|FSC_\lambda| / (1 - |FSC_\lambda|)$ [9, 28, 42]). Since we do not generally have ground truth density maps for real experimental datasets, FSC between ground truth and estimated maps is typically only used with synthetic data, e.g. CryoBench [15].

For homogeneous reconstruction with real experimental data, where ground truth is unavailable, FSC is used as a measure of consistency between two ‘independent’ 3D reconstructions. In the “gold standard” protocol, one randomly divides the set of particle images into halves, from which one estimates two 3D density maps that we assume are conditionally independent given the true density. FSC then provides a measure of consistency as a function of frequency between the two half-maps. When using the gold standard FSC protocol (comparing two half-maps estimated from independent halves of the data), a threshold of 0.143 is used to measure the map resolution, which approximately corresponds to when the spectral SNR of a map computed from the full set of images is 1 [36].

Despite the widespread use of FSC with the gold standard protocol, there is no accepted extension to heterogeneous reconstruction. The best existing benchmark, namely CryoBench [15], leverages synthetic data, in which case one has ground truth density maps available. To handle heterogeneity, they define the Per-Conformation FSC metric as the average AUC-FSC or FSC curve taken over all ground truth states generated in the synthetic dataset, whether compositional or conformational in its heterogeneity. This is the performance metric reported in Table 1 and Figure 3. A closely related measure is the Per-Image FSC, which is the mean AUC-FSC between the ground truth density maps and those estimated from the latent state by taking one sample particle per ground-truth state. For completeness we report this below in Table 3 and visualize FSC curves in Fig. 10. Due to the high memory requirements, we were unable to reproduce FSC curves for RECOVER by the time of submission. For more details on RECOVER performance, see the CryoBench paper [15].

Method	IgG-1D		IgG-RL		Ribosembly	
	Mean (std)	Med	Mean (std)	Med	Mean (std)	Med
3D Classification [39]	0.297 (0.019)	0.291	0.309 (0.01)	0.307	0.289 (0.081)	0.288
CryoDRGN [47]	0.351 (0.028)	0.356	0.331 (0.016)	0.333	0.412 (0.023)	0.415
CryoDRGN-AI-fixed [19]	0.364 (0.002)	0.364	0.348 (0.012)	0.350	0.372 (0.032)	0.375
3DFlex [33]	0.335 (0.003)	0.335	0.337 (0.007)	0.337	-	-
3DVA [32]	0.349 (0.004)	0.350	0.333 (0.014)	0.335	0.375 (0.038)	0.375
RECOVAR [10]	0.386 (0.001)	0.388	0.363 (0.011)	0.363	0.429 (0.018)	0.432
CryoSPIRE (Ours)	0.396 (0.013)	0.400	0.375 (0.020)	0.391	0.422 (0.015)	0.421

Table 3: Mean AUC of **Per-Image FSC** is reported for various methods on CryoBench datasets [15]. In parentheses, we report the standard deviation indicating the spread of AUC among different structural states (100 states for IgG-1D and IgG-RL and 16 states for Ribosembly). FSC curves are computed after masking out background noise. We AUC numbers from CryoBench [15] for RECOVAR. (Best method in bold, second best underlined.)

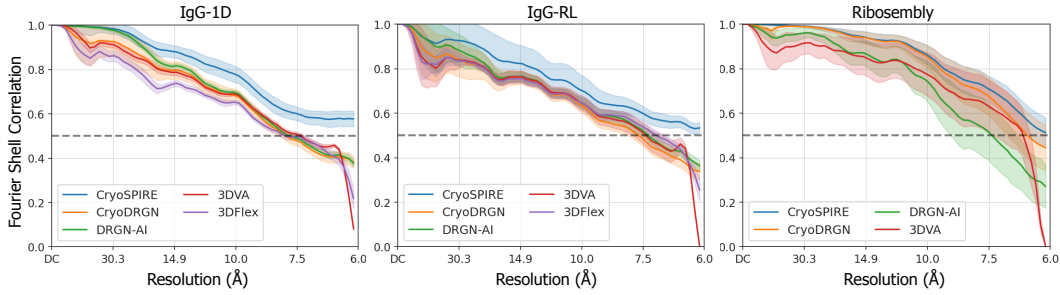


Figure 10: Per-Image FSCs on CryoBench datasets. Error bars indicate standard deviation across different states. The highest possible resolution is 6 Å on these synthetic datasets.

E Complete Qualitative Result on Ribosembly

While Figure 6 in the main body of the paper shows example compositional states reconstructed by CryoSPIRE, Figure 11 shows all 16 states.

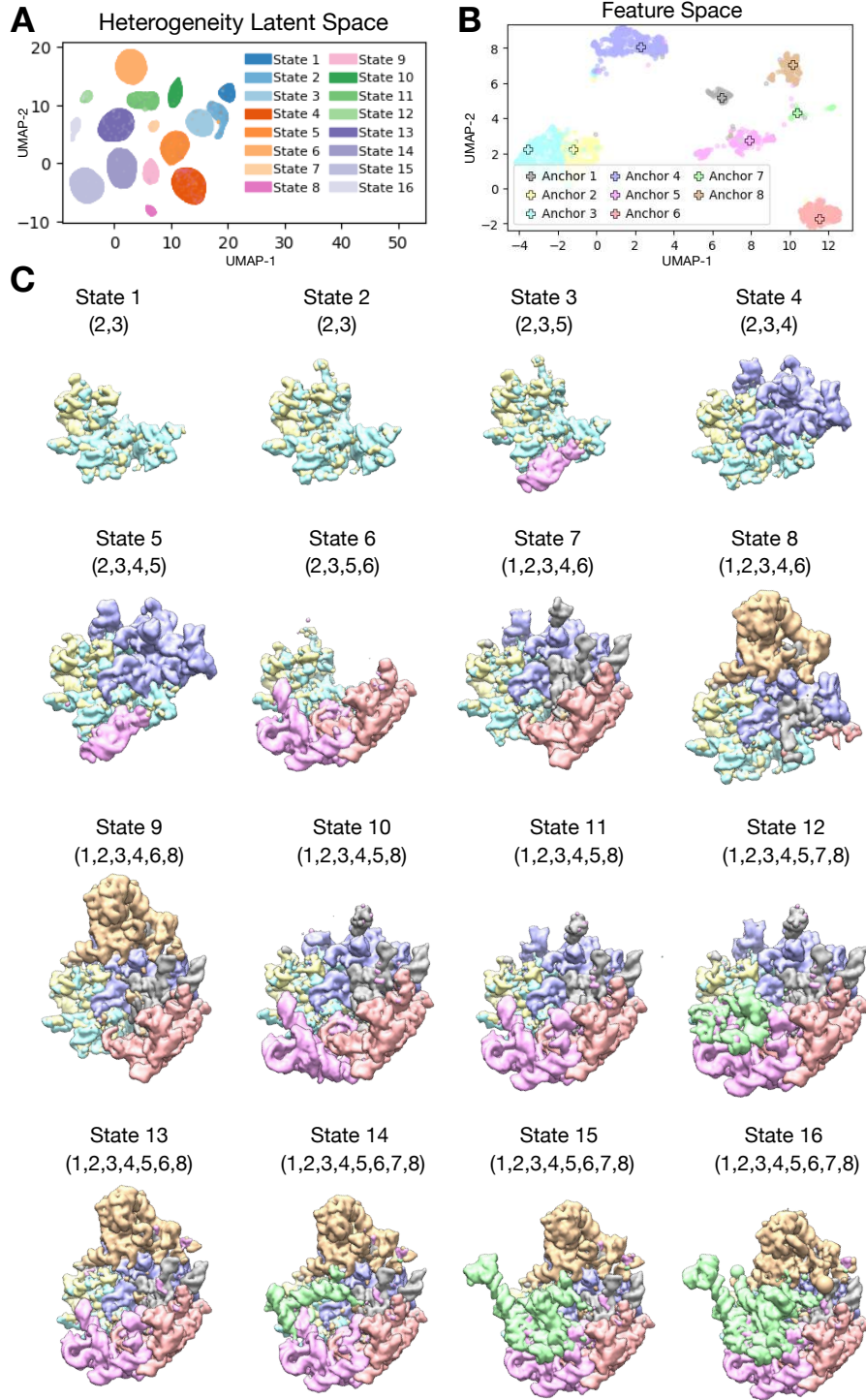


Figure 11: Complete qualitative results on Ribosembly [15] (A) Gaussian feature space, \mathfrak{F} , showing eight major parts identified through clustering. (B) Heterogeneity latent space, \mathfrak{Z} , colored coded with the ground-truth compositional state. (C) Visualizations of all 3D density maps corresponding to 16 compositional states, with colors depicting parts (given in parentheses).

F Qualitative Comparisons on CryoBench Data

In Figures 4, 5 and 6, we showed qualitative result of CryoSPIRE on CryoBench synthetic datasets of IgG-1D, IgG-RL and Ribosembly, respectively. Here, in Figure 12, we compare CryoSPIRE with the state-of-the-art methods 3DFlex [33], 3DVA [32], CryoDRGN [47], DRGN-AI [19], and with ground-truth structural states. Please find detailed 3D visualizations of the reconstruction in the webpage.

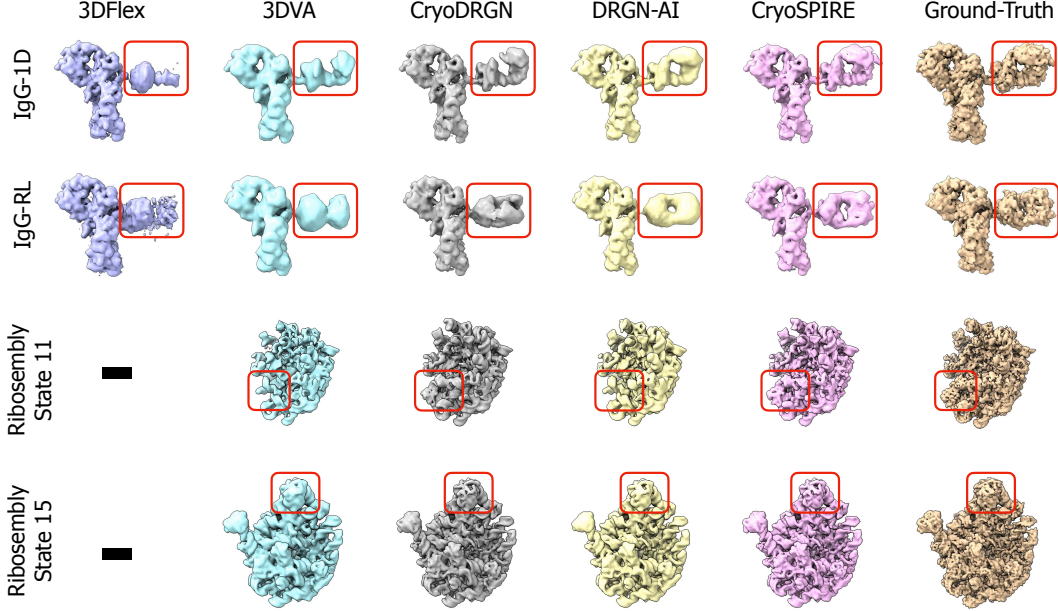


Figure 12: Qualitative comparison of CryoSPIRE with four state-of-the-art methods on CryoBench synthetic datasets [15]. Last column corresponds to the ground-truth state. In the first two rows, reconstruction of all methods for a sample conformational state is provided for IgG-1D and IgG-RL, demonstrating that our method outperforms others in recovering higher frequency details in the Fab domain (highlighted in red). For Ribosembly, we provide reconstructions of two example compositional states (labeled as 11 and 15). Since 3DFlex is limited to conformational heterogeneity, it is not evaluated on this dataset. Reconstructions of the state 11 by DRGN-AI and 3DVA clearly miss a subunit, while CryoSPIRE is able to capture it. Moreover, for state 15, DRGN-AI and 3DVA are overall less detailed while CryoSPIRE appears slightly better than CryoDRGN. 3D visualizations of the above reconstructions are presented in the webpage.

G Qualitative Comparisons on Experimental datasets

Figures 7 and 8 in the main body of the paper showed qualitative result of CryoSPIRE on Large Ribosomal Subunit (EMPIAR-10076 [7]) and Pre-Catalytic Spliceosome (EMPIAR-10180 [30]), respectively. Here, in Figs 13 and 14, we show comparisons with state-of-the-art methods 3DVA [32] and CryoDRGN [47] and 3DFlex [33]. As these Ribosome data mainly exhibit compositional heterogeneity, 3DFlex is not evaluated on this dataset. For both 3DVA and 3DFlex, we use CryoSPARC v4.4.0 [34] with default setting. We use the default 3 variability components for 3DVA, while for 3DFlex, we run *3DFlex Training Job*, followed by *3DFlex Reconstruction* to obtain a high-resolution canonical structure. For CryoDRGN, we use the final result provided by the authors. Please find detailed 3D visualizations of the reconstruction in the webpage.

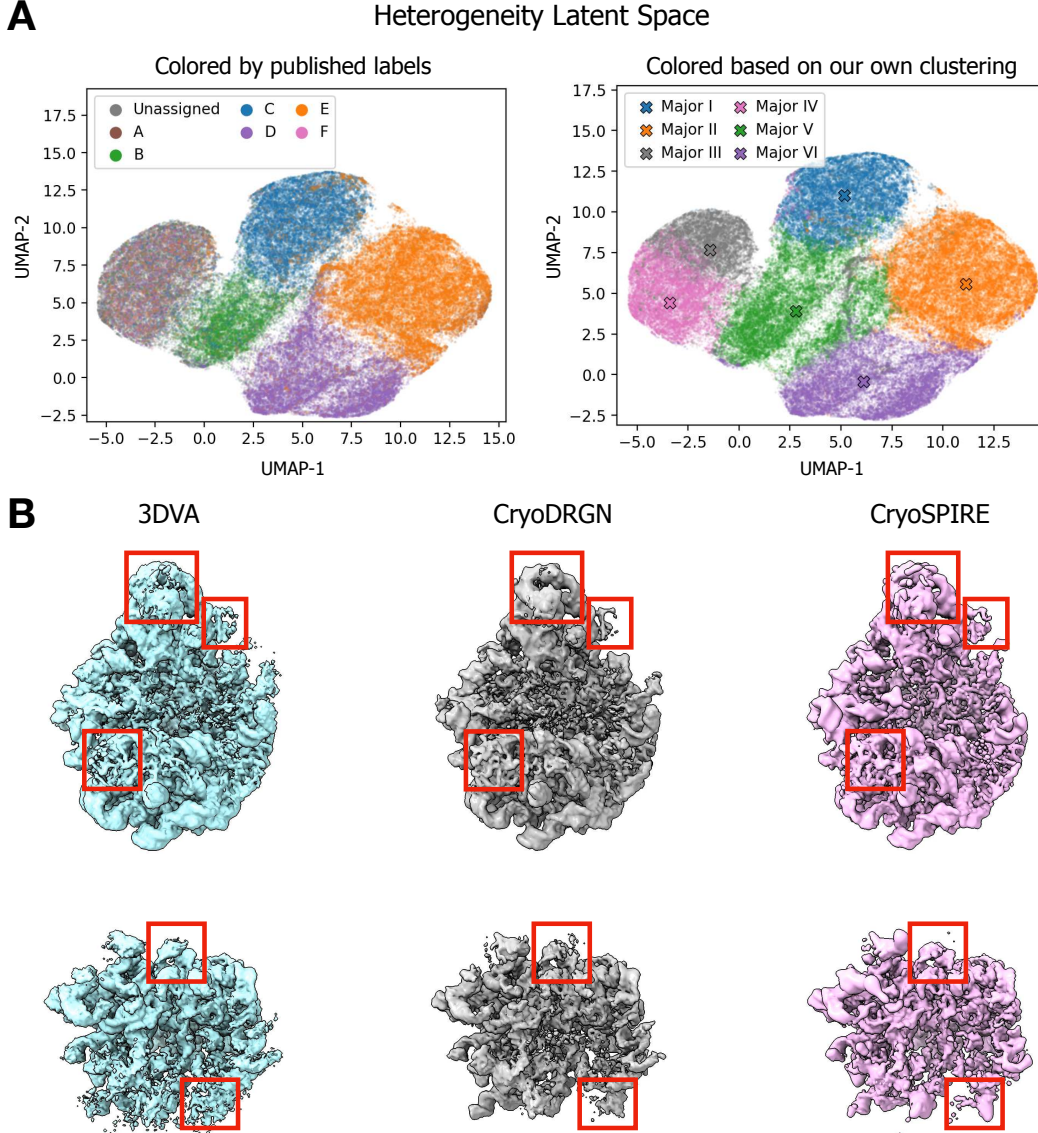


Figure 13: More qualitative result on Large Ribosomal Subunit (EMPIAR-10076 [7]) (A) Heterogeneity latent space, with latent points colored based on the published labels [7] (left) and colored based on our own clustering of latent space (right). (B) Qualitative comparison of CryoSPIRE with 3DVA [32] and CryoDRGN [47]. Two rows shows two of major assembly states. We identify some areas with red rectangles that shows main discrepancies between different methods. 3D visualizations of the above reconstructions are presented in the webpage.

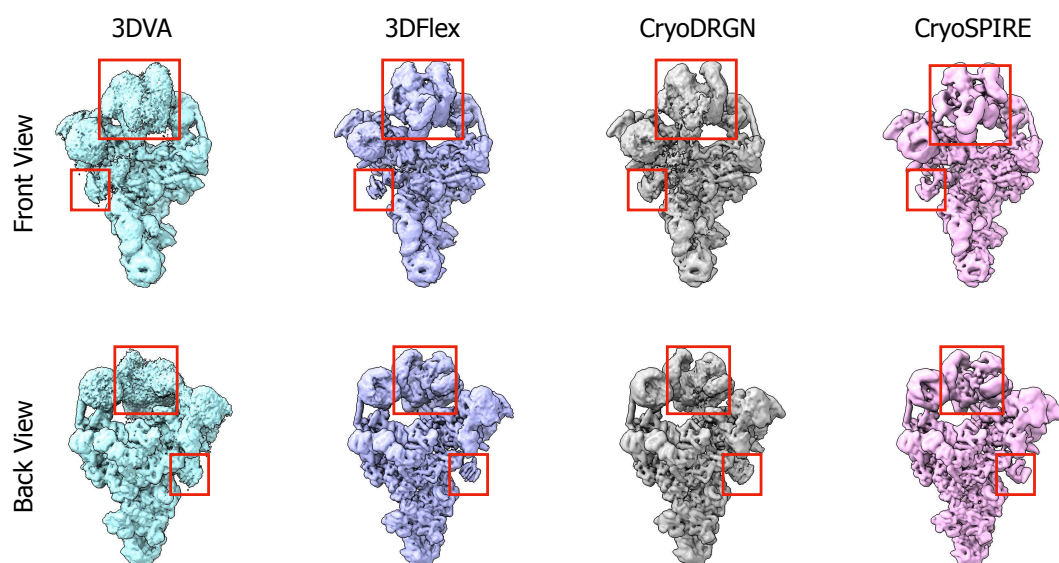


Figure 14: Qualitative comparison of CryoSPIRE with 3DVA [32], 3DFlex [33] and CryoDRGN [47] on Pre-Catalytic Spliceosome (EMPIAR-10180 [30]). Two rows show front and back views of the reconstructions, respectively. In both views, we mark the SF3b and a peripheral subunit of helicase with red rectangles. The reconstructions obtained by 3DVA, 3DFlex and CryoDRGN contain high-frequency noise within the two marked areas, whereas our method is better in resolving corresponding regions. 3D visualizations of the above reconstructions are presented in the webpage.